

## Article

# Two 5-Methoxyindole Carboxylic Acid-Derived Hydrazones of Neuropharmacological Interest: Synthesis, Crystal Structure, and Chemiluminescent Study of Radical Scavenging Properties

Neda Anastassova <sup>1,2</sup>, Nadya Hristova-Avakumova <sup>3</sup>, Rusi Rusew <sup>4</sup> , Boris Shivachev <sup>4</sup>  and Denitsa Yancheva <sup>1,2,\*</sup> 

<sup>1</sup> Institute of Organic Chemistry with Centre of Phytochemistry, Bulgarian Academy of Sciences, Acad. G. Bonchev Str., Building 9, 1113 Sofia, Bulgaria; neda.anastassova@orgchm.bas.bg

<sup>2</sup> Department of Organic Chemistry, University of Chemical Technology and Metallurgy, 8 Kliment Ohridski Blvd., 1756 Sofia, Bulgaria

<sup>3</sup> Department of Medical Physics and Biophysics, Faculty of Medicine, Medical University of Sofia, 2 Zdrave Str., 1431 Sofia, Bulgaria; nrhristova@medfac.mu-sofia.bg

<sup>4</sup> Institute of Mineralogy and Crystallography “Acad. Ivan Kostov”, Bulgarian Academy of Sciences, Acad. G. Bonchev Str., Bl. 107, 1113 Sofia, Bulgaria; r.rusev93@gmail.com (R.R.); blshivachev@gmail.com (B.S.)

\* Correspondence: denitsa.pantaleeva@orgchm.bas.bg



**Citation:** Anastassova, N.; Hristova-Avakumova, N.; Rusew, R.; Shivachev, B.; Yancheva, D. Two 5-Methoxyindole Carboxylic Acid-Derived Hydrazones of Neuropharmacological Interest: Synthesis, Crystal Structure, and Chemiluminescent Study of Radical Scavenging Properties. *Crystals* **2024**, *14*, 396. <https://doi.org/10.3390/crust14050396>

Academic Editor: Tom Leyssens

Received: 31 March 2024

Revised: 19 April 2024

Accepted: 22 April 2024

Published: 25 April 2024



**Copyright:** © 2024 by the authors. Licensee MDPI, Basel, Switzerland. This article is an open access article distributed under the terms and conditions of the Creative Commons Attribution (CC BY) license (<https://creativecommons.org/licenses/by/4.0/>).

## 1. Introduction

Indole core is a natural bioactive fragment present in the amino acid tryptophan, the hormones melatonin and serotonin, the tryptophan-derived compounds indole-3-propionic acid (IPA), indole-3-propionamide (IPAM), and indole-3-carbaldehyde (I3A), produced biosynthetically in gut microbiota [1,2], and is present in various alkaloids from plants, fungi, sponges, tunicates, and bryozoans [3–8]. The indolyl fragment is part of the structure of some commercial drugs and controlled substances as well—the antiarrhythmic drug ajmaline [9], physostigmine used for anticholinergic poisoning treatment [10] and the

antimitotic agent vincristine [11], the psychoactive compounds ibogaine, psilocybin, and LSD [12].

The indole molecules produced by gut microbiota have been shown to possess important biological activities, including neuroprotection and antioxidant properties, anti-inflammatory, immunoregulatory, and amyloid anti-aggregation properties [13–17]. Further research has attested to the beneficial effects of some of the bacteria-produced indole compounds on the age of onset and the progression of Alzheimer’s disease [18]. It was suggested that stimulating the microbiota to higher production of neuroprotective indoles can promote brain health during ageing and lower the risk of dementia development [18]. In terms of neutralizing free radicals, IPA and IPAM are believed to be twice as potent as melatonin [19]. They neutralise the highly reactive hydroxyl radicals via electron donation and in contrast to antioxidants, such as ascorbic acid (vitamin C), tocopherol (vitamin E), and other chain-breaking free-radical scavengers, do not generate prooxidant intermediates while neutralizing free radicals [19]. 5-Methoxyindole-2-carboxylic acid (5MICA) has also shown beneficial neuroprotective action against ischemic stroke injury and functional improvements after stroke in rats [20]. 5MICA has reduced infarct size, improved oxidative stress status, and improved long-term potentiation [20]. 5MICA acts as an inhibitor of the mitochondrial dihydrolipoamide dehydrogenase (DLDH), which also contributes to the chemical preconditioning and neuroprotection against ischemic injury [21,22].

The great potential of indole core for the development of neuroprotective agents prompted us recently to synthesise a series of benzaldehyde hydrazone derivatives of 5MICA that showed promising neuroprotective effects, a favourable safety profile in human neuroblastoma SH-SY5Y, and mouse brain endothelial cell bEnd3 cell lines, in addition to human recombinant monoamine oxidase-B (hMAO-B) enzyme inhibition and radical scavenging activity [23]. The dihydroxybenzaldehyde and 2-hydroxy-4-methoxybenzaldehyde derivatives of 5MICA demonstrated some of the strongest neuroprotective effects in H<sub>2</sub>O<sub>2</sub>-induced oxidative stress on SH-SY5Y cells and 6-hydroxydopamine (6-OHDA)-induced neurotoxicity in rat brain synaptosomes. Furthermore, all compounds suppressed iron-induced lipid peroxidation. The hydroxyl derivatives also exhibited the highest activity in deoxyribose degradation inhibition and superoxide anion generation.

Considering the pivotal role of molecular structure in pharmacological activity and interaction with biological receptors, a study on the 3,4-dihydroxybenzaldehyde hydrazone derivative of 5MICA and a newly synthesised analogue bearing a 2-methoxy-4-hydroxyphenyl ring was conducted using single-crystal X-ray diffraction. The crystallographic study gave insight into the molecular structure, rotation and deformation freedom of the respective indole, phenyl fragments, and adjacent functional groups, as well as specific interactions stabilizing the three-dimensional packing of the molecules in the crystal structures, such as hydrogen bonding, short contacts, and π–π stacking. More insights into the influence of the molecular structure of **3a** and **3b** on their biological properties were gained via *in vitro* evaluation of the radical scavenging ability towards different reactive oxygen species (ROS). The luminol-dependent chemiluminescence was monitored in model systems of NaOCl, K<sub>2</sub>O<sub>2</sub>-produced superoxide, and xanthine—xanthine oxidase-generated superoxide radicals. In the next phase of this study, the potential for the two derivatives to modulate oxidative damage induced by iron on biologically significant molecules, such as lecithin and deoxyribose, and to exhibit antioxidant or prooxidant effects was assessed and compared.

## 2. Materials and Methods

### 2.1. Materials

Melting points (mps) were determined utilizing a Büchi B-540 instrument (Büchi, Flawil, Switzerland) and are reported without correction. ATR IR spectra were captured on a Bruker Invenio R spectrometer equipped with a diamond ATR accessory, employing 64 scans at a resolution of 2 cm<sup>-1</sup>. The 1H and 13C NMR spectra were acquired on Bruker Neo 600 MHz and Bruker Neo 400 MHz NMR instruments, respectively. The spectra

were referenced to the solvent signal, with chemical shifts expressed in ppm and coupling constants in Hz. The mass spectra are recorded using a Q Exactive Plus Hybrid Quadrupole-Orbitrap Mass Spectrometer Thermo Scientific (HESI HRMS) (Thermo Fisher Scientific, MA, USA) in negative mode. The spectra were processed using the Thermo Scientific FreeStyle program version 1.8 SP1 (Thermo Fisher Scientific Inc., Waltham, MA, USA). The progress of reactions was monitored via thin layer chromatography carried out on Merck pre-coated plates (silica gel, 60 F254, 0.25 mm), visualised by fluorescence quenching under UV light (254 nm). Melting points and spectral data are exclusively provided for the novel target compounds **3a** and **3b**.

## 2.2. Synthesis

The synthesis of the hydrazide from the methyl ester of 5-methoxy-1H-indole-2-carboxylic acid has been published elsewhere [23].

Either 2.0.5 mmol (1.0 equiv.) of 3,4-dihydroxybenzaldehyde (for compound **3a**) or 0.5 mmol 4-hydroxy-2-methoxybenzaldehyde (for compound **3b**) was added to a solution of hydrazide 2 (0.5 mmol) in absolute ethanol. The reaction mixture was refluxed for 2 h. Progress of the reaction was monitored using TLC with a solvent system of benzene:methanol (4:1). Upon completion, the mixture was concentrated under reduced pressure. The resulting precipitate was filtered and washed with cool ethanol. The compounds were further purified by recrystallisation with ethanol, and their purity was confirmed by TLC, IR, and <sup>1</sup>H NMR spectroscopy. Detailed ATR-IR and NMR spectra are provided in the Supplementary Materials.

### *N'-(3,4-dihydroxybenzylidene)-5-methoxy-1H-indole-2-carbohydrazide (**3a**)*

Yield 85%, Mp 252–253 °C, IR ( $\nu_{\text{max}}/\text{cm}^{-1}$ ) IR ( $\nu_{\text{max}}/\text{cm}^{-1}$ ) 3307 ( $\nu\text{O-H}$ ); 3262 ( $\nu\text{N-H}$ ); 2936 ( $\nu_{\text{as}}\text{CH}_2$ ); 2840 ( $\nu_{\text{s}}\text{CH}_2$ ); 1620 ( $\nu\text{C=O}$ ) amide I; 1604 ( $\nu\text{C=N}$ ); 1565 ( $\delta\text{N-H}$ ); 1248 ( $\nu\text{C-O-C}$ ); <sup>1</sup>H NMR (400 MHz, DMSO-*d*<sub>6</sub>)  $\delta$ , ppm: 11.65 (s, 1H, NH), 11.57 (s, 1H, NH), 9.51 (s, 1H, OH), 9.36 (s, 1H, OH), 8.24 (s, 1H, CH),  $\delta$  7.37–7.35 (d,  $J$  = 8.9 Hz, 1H), Ar-H), 7.26–7.25 (d,  $J$  = 2.0 Hz, 1H, Ar-H), 7.18–7.11 (m, 2H, Ar-H), 6.99–6.96 (dd,  $J$  = 8.2, 2.0 Hz, 1H, Ar-H), 6.99–6.96 (dd,  $J$  = 8.9, 2.4 Hz, 1H, Ar-H), 6.81–6.79 (m, 1H, Ar-H), 3.77 (s, 3H, OCH<sub>3</sub>). <sup>13</sup>C NMR (151 MHz, DMSO-*d*<sub>6</sub>) 57.90, 154.34, 148.41, 148.11, 146.19, 132.52, 132.03, 130.96, 126.26, 121.06, 116.07, 115.50, 114.79, 113.70, 113.55, 113.16, 103.44, 102.46, 102.18, 55.73. *m/z* M-H = 324.0989.

### *N'-(4-Hydroxy-2-methoxybenzylidene)-5-methoxy-1H-indole-2-carbohydrazide (**3b**)*

Yield 90%, Mp 243–244 °C, IR ( $\nu_{\text{max}}/\text{cm}^{-1}$ ) 3304 ( $\nu\text{O-H}$ ); 3246 ( $\nu\text{N-H}$ ); 2920 ( $\nu_{\text{as}}\text{CH}_3$ ); 2849, 2828 ( $\nu_{\text{s}}\text{CH}_3$ ); 1600 ( $\nu\text{C=O}$ ) amide I; 1608 ( $\nu\text{C=N}$ ); 1560 ( $\delta\text{N-H}$ ); 1255 ( $\nu\text{C-O-C}$ ). <sup>1</sup>H NMR (400 MHz, DMSO-*d*<sub>6</sub>)  $\delta$ , ppm: 11.66 (s, 1H, NH), 11.54 (s, 1H, NH), 10.10 (s, 1H, OH), 8.66 (s, 1H, CH), 7.74–7.72 (d,  $J$  = 8.9 Hz, 1H, Ar-H), 7.35–7.33 (d,  $J$  = 8.8 Hz, 1H, Ar-H), 7.19 (s, 1H, Ar-H), 7.10 (s, 1H, Ar-H), 6.87–6.84 (dd,  $J$  = 8.9, 2.4 Hz, 1H), 6.47–6.45 (m, 2H, Ar-H), 3.81 (s, 3H, CH<sub>3</sub>), 3.76 (s, 3H, CH<sub>3</sub>). <sup>13</sup>C NMR (151 MHz, DMSO-*d*<sub>6</sub>)  $\delta$ , ppm: 161.45, 159.78, 157.77, 154.34, 143.38, 132.51, 131.04, 127.86, 127.32, 115.43, 114.03, 113.66, 108.81, 103.37, 102.52, 99.44, 55.97, 55.76. HRMS (ESI) *m/z*: M-H = 338.1146.

## 2.3. Single-Crystal X-ray Diffraction (SCXRD)

Suitable single crystals of compounds **3a** and **3b** with appropriate size (dimensions: 0.3 × 0.2 × 0.2 mm<sup>3</sup>) and without visible defects were mounted on nylon loops using cryoprotective oil. Diffraction data were collected at 290 K on a Bruker D8 Venture diffractometer equipped with an  $\mu$ S micro-focus sealed Mo X-ray source ( $\lambda$  = 0.71073 Å) and PHOTON II CPAD detector using APEX4 ver. 2021.10.0 [24] as data acquisition and processing software. Data reduction (integration and scaling) was performed with Bruker SAINT ver. 8.40B [25], and the data were corrected for absorption effects using multi-scan method (SADABS ver. 2016/2 [25]). The crystal structures of **3a** and **3b** were solved with Intrinsic Phasing method and were refined with Least-Squares minimisation using ShelxT [26] and ShelxL [27] programs, respectively, integrated in OLEX2-ver. 1.5 software [28]. All non-

hydrogen atoms (C, N, O) were located successfully from Fourier map and were refined anisotropically. Hydrogen atoms attached to carbon were placed on calculated positions using the following scheme:  $U_{eq} = 1.2$  for C–H aromatic groups (0.93 Å) and  $U_{eq} = 1.5$  for C–H methyl groups (0.96 Å). Hydrogen atoms riding on O and N atoms were refined from electron density maps. Ortep-3v2 software [29] was used to visualise the molecules of 1 and 2 in the asymmetric unit (ASU). CCDC Mercury v4.0 [30] was used to prepare the figures illustrating the detected hydrogen bonding interactions,  $\pi$ – $\pi$  stacking, and three-dimensional packing for **3a** and **3b**. Crystal data and structure refinement parameters are given in Table S1. Values for bond lengths and angles are given in Tables S2–S5. The detected hydrogen bonding interactions and short contacts are summarised in Table 1. Complete crystallographic data for the reported structures **3a** and **3b** were deposited in the CIF format with the Cambridge Crystallographic Data Centre, ref. codes 2342743 and 2342744. These data can be obtained free of charge via [www.ccdc.cam.ac.uk/structures](http://www.ccdc.cam.ac.uk/structures) (accessed on 24 March 2024).

**Table 1.** Detected hydrogen bonding interactions and short contacts for **3a** and **3b**.

Compound <b>3a</b>						
D	H	A	d(D-H)/Å	d(H-A)/Å	d(D-A)/Å	D-H-A/°
N14	H14	O24 <sup>1</sup>	0.91(3)	2.08(3)	2.870(2)	145(2)
N1	H1	O10 <sup>2</sup>	0.91(3)	2.10(3)	2.996(2)	167(2)
O23	H23	O13 <sup>3</sup>	0.98(4)	1.82(4)	2.793(2)	168(3)
O24	H24	O13 <sup>3</sup>	0.98(2)	1.71(2)	2.684(2)	177(3)

Compound <b>3b</b>						
D	H	A	d(D-H)/Å	d(H-A)/Å	d(D-A)/Å	D-H-A/°
C32	H32	O231 <sup>2</sup>	0.93	2.57	3.410(3)	150.3
C191	H191	O102 <sup>4</sup>	0.93	2.66	3.467(3)	146.1
C211	H211	N152	0.93	2.72	3.634(2)	166.4
O231	H231	O132	0.98(3)	1.67(3)	2.642(2)	170.0 (2)
O232	H232	O131 <sup>3</sup>	0.94(4)	1.88(4)	2.782(2)	158.0(3)
N141	H141	O232 <sup>1</sup>	0.91(2)	2.18(2)	3.031(2)	155.2(2)
N142	H142	O231 <sup>2</sup>	0.94(2)	2.04(2)	2.966(2)	165.0(2)
N12	H12	O132 <sup>5</sup>	0.89(2)	2.04(2)	2.879(2)	157.0(2)
N11	H11	O131 <sup>6</sup>	0.88(2)	2.08(2)	2.869(2)	148.1(2)

Symmetry operations: <sup>1</sup> +X, 1+Y, +Z; <sup>2</sup> 1+X, +Y, +Z; <sup>3</sup> 1+X, –1+Y, +Z; <sup>4</sup> 1–X, 2–Y, 1–Z; <sup>5</sup> 1–X, 1–Y, 1–Z; <sup>6</sup> –X, 2–Y, 2–Z
--

Hirshfeld surface analysis (HSA) for compounds **3a** and **3b** was performed with CrystalExplorer 21.5 [31,32]. The computed surface properties in CrystalExplorer were generated from the crystal structure file (CIF) using experimental crystal geometries (no additional optimisation of the molecular geometries was performed). The corresponding interaction energies were calculated for all unique molecular pairs observed in **3a** and **3b** at CEB3LYP, B3LYP/6-31G(d,p) level using Tonto [33]. A molecular electrostatic potential (MEP) map was plotted to detect the nucleophilic and electrophilic properties of **3a** and **3b**. The local reactivity of the complex containing nucleophilic and electrophilic attacking sites was forecasted using Mulliken atomic charge distribution on atoms. Furthermore, the HOMO-LUMO (highest occupied molecular orbital-lowest unoccupied molecular orbital) surfaces were represented in order to assess the reactivity of the compounds.

#### 2.4. Radical Scavenging Assays

Chemiluminescent determination of the radical scavenging activity against different types of ROS and estimation of the antioxidant properties in spectrophotometric model systems containing biologically important molecules were performed.

#### 2.4.1. Chemiluminescent Radical Scavenging Assays

The application of chemiluminescent studies is widespread in biochemical laboratories and clinical research. These methods have been acknowledged for their reliability and sensitive methodologies, with a  $10^{-19}$  M detection threshold and a wide linear range extending over approximately two decades [34–37]. Our study used luminol-dependent chemiluminescence to determine the scavenging activity against the superoxide anion radical ( $O_2^{\bullet-}$ ) and the hypochlorite ion ( $OCl^-$ ). The experiments were performed using an LKB 1251 chemiluminometer (Bioorbit, Turku, Finland) connected to an IBM-PC-compatible computer via serial port. Data collection and analysis were carried out using the MultiUse program Version 1.08 (Bioorbit), with measurements conducted at 37 °C in three different model systems. For each assay, “Control” measurement compositions that did not contain the investigated derivatives and “Sample” compositions containing different concentrations of the hydrazone were prepared. Each run of samples included a blank sample representing a negative control. This background signal was subtracted from both “Control” and “Samples”. The chemiluminescent response was evaluated by calculating the area under the generated chemiluminescent curve. The chemiluminescence (CL) ratio in the presence/absence of the investigated compound expressed as a percentage was termed the chemiluminescent scavenging index (CL-SI). This index was used to determine and compare the scavenging properties of the derivatives.

Assay I involved luminol-dependent chemiluminescence in a system of sodium hypochlorite-derived hypochlorite. Samples of 1 mL phosphate-buffered saline (PBS), containing 0.1 mM luminol, 0.06 NaOCl, and the tested derivatives at the desired concentration were prepared. Control samples were prepared without the inclusion of the studied compounds. The chemiluminescent signal was registered for 1 min at intervals of 50 milliseconds after the addition of NaOCl.

Assay II involved luminol-dependent chemiluminescence in a system of potassium superoxide-derived superoxide anion radicals ( $O_2^{\bullet-}$ ). Samples of 1 mL containing 50 mM PBS at pH 7.4, 0.1 mM luminol, and the studied compounds were prepared. In the control samples, hydrazones were omitted. The chemiluminescence response was instantly measured after adding 20  $\mu$ L KO<sub>2</sub> (dissolved in DMSO) and registered for 1 min at intervals of 50 milliseconds.

Assay III involved luminol-dependent chemiluminescence in a system of xanthine—xanthine oxidase-generated superoxide radicals. Samples of 1 mL PBS, containing 0.1 mM luminol, 1 mM xanthine, and the investigated compounds at the concentrations indicated in the figures were prepared. In the control measurements, the derivatives were omitted. Xanthine oxidase (20  $\mu$ L–100 IU/L in PBS) was added to each sample and control, and subsequently, the CL signal was measured for 5 min.

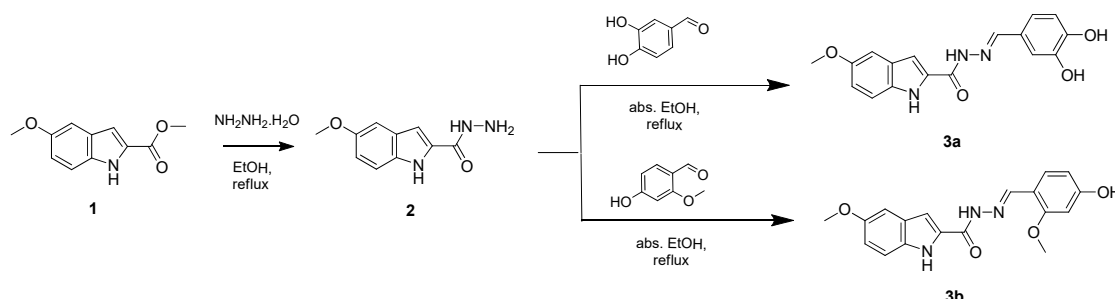
#### 2.4.2. Thiobarbituric Acid Reactive Substances (TBA-RS)

We employed ferrous irons to investigate the peroxidation of biologically relevant molecules [34]. The effects of the tested hydrazone derivatives on *in vitro* Fe(II)-induced oxidative damage in lecithin containing system were investigated at a concentration of 90  $\mu$ M, while in the deoxyribose degradation assay, an 80  $\mu$ M concentration was used in accordance with our prior studies [23,38]. For this purpose, 1 mL samples of phosphate buffer (PB, 7.4), comprising 1 mg of lecithin per mL or 2-Deoxyribose [0.5 mM], were prepared [39–41]. FeCl<sub>2</sub> at a concentration of 0.1 mM was applied to initiate oxidative damage. Subsequently, all measurement compositions underwent incubation at 37 °C for 30 min. In the next step, 0.5 mL of 2.8% trichloroacetic acid and 0.5 mL of thiobarbituric acid were added. All measurement compositions were heated in a boiling water bath at 100 °C for 20 min and then centrifuged at 3000 rpm for 20 min. Determination of the absorbance at 532 nm was performed.

### 3. Results and Discussion

#### 3.1. Synthesis

The synthesis of the two arylhydrazone 5-methoxyindole-2-carboxylates was conducted following the procedure outlined in Scheme 1. The methyl ester of 5-methoxyindole carboxylic acid **1** was subjected to hydrazinolysis with hydrazine hydrate in ethanol, affording hydrazide **2**. Subsequent condensation with the respectively substituted benzaldehydes led to the formation of the two target compounds, **3a** and **3b**. Structural elucidation of the products was confirmed with comprehensive analyses utilizing IR and NMR spectroscopy techniques.



**Scheme 1.** Synthesis of arylhydrazone 5-methoxyindole-2-carboxylates.

#### 3.2. Crystal Structure Description

Colourless crystal blocks of compounds **3a** and **3b** were obtained by slow evaporation from an ethanol solution. Compounds **3a** and **3b** crystallised in the monoclinic  $P2_1/c$  and the triclinic  $P-1$  space groups with one or two independent molecules in the ASU ( $Z' = 1$  or  $2$ ), respectively, and a total of four molecules in the unit cell ( $Z = 4$ ). The ORTEP view [29] of the molecules of **3a** and **3b** present in the ASU, with an appropriate atom-numbering scheme, is given in Figure 1.

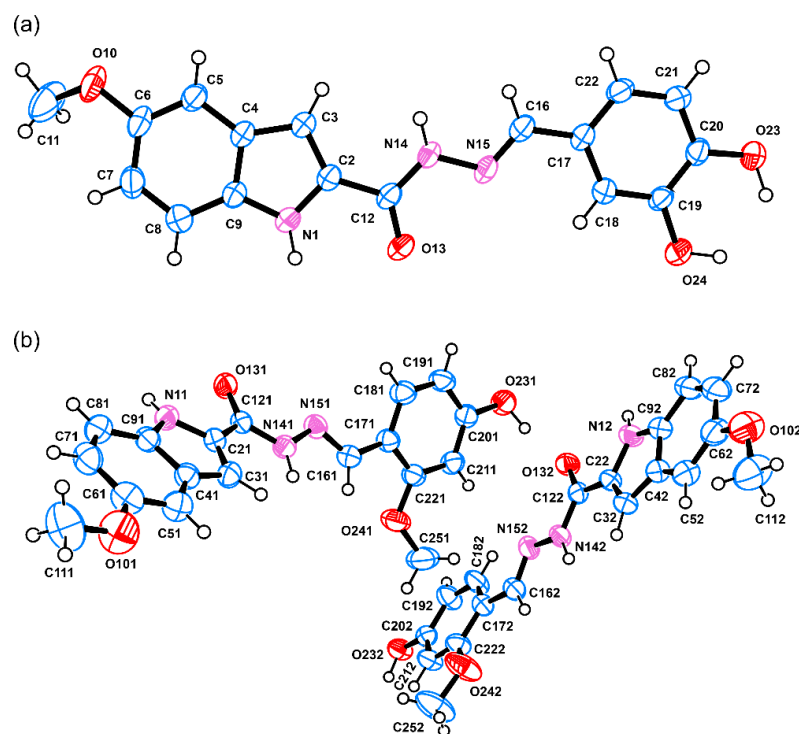


**Figure 1.** ORTEP view of the molecules present in the ASU of (a) compound **3a** and (b) compound **3b** with appropriate atom-numbering scheme. Thermal ellipsoids (atomic displacement parameters) are given at the 50% probability level.

The molecules of **3a** and **3b** feature common 5-methoxy-1*H*-indole and corresponding 3,4-dihydroxybenzene (for **3a**) and 4-hydroxy-2-methoxy benzene (for **3b**) moieties connected by a shared  $-\text{C}(=\text{O})\text{--NH--N=CH--}$  bridge. The conjugated indole fragment in both **3a** and **3b** is relatively planar with root mean square deviation (RMSD) values of 0.012 Å for **1** and 0.009/0.010 Å for the two independent molecules in **3b**, respectively. The same is valid for the phenyl rings in the respective 3,4-dihydroxybenzene (0.011 Å) and 4-hydroxy-2-methoxy benzene—0.004/0.006 Å. Considering the methoxy groups, noticeable deviation from planarity is observed, e.g., RMSD of 0.171 Å for the 5-methoxy-1*H*-indole fragment in **3a** and 0.035/0.053 Å for the 4-hydroxy-2-methoxy benzene fragment in both independent molecules of **3b**. It is expected that the presence of  $-\text{C}(=\text{O})\text{--NH--N=CH--}$  bridge will increase the overall flexibility of the molecules of **3a** and **3b**. However, **3a** has highly conserved geometry and limited rotation and deformation freedom of the respective indole and phenyl fragments with values for the twist and fold angles between their mean planes of 7.33° and 3.91°. The same is valid for the conjugated indole/phenyl rings in one of the independent molecules in **3b** (namely N12-C22-C32-C42-C52-C62-C72-C82-C92/C172-C182-C192-C202-C212-C222), with twist and fold angles of 9.47° and 5.07°. Interestingly, the other independent molecule in the ASU of **3b** deviates from this trend with twist and fold angles of 125.97° and 164.10°. Those conformational differences between the two independent molecules in **3b** and the molecule of **3a** vs. **3b** are clearly visible from the overlay by their common indole fragment (Figure 2).

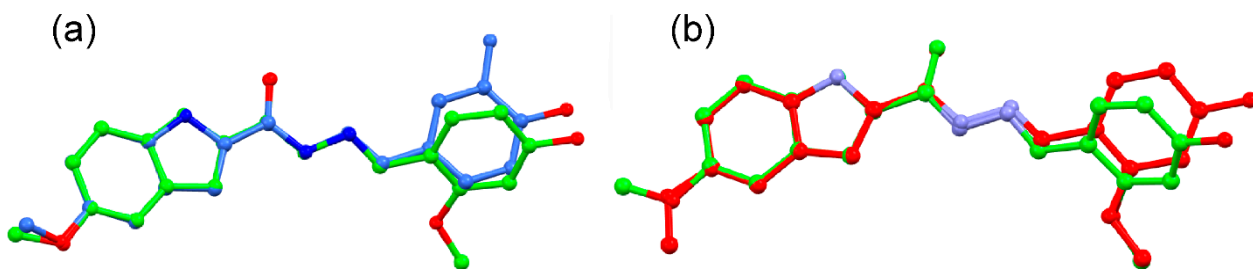


**Figure 2.** Overlay of the molecules of (a) **3a** (in blue) and **3b** (in green) and (b) the two independent molecules in the ASU of **3b** by their common indole fragment, emphasizing their conformational differences; the RMSDs are 0.721 and 0.627 Å, respectively. Hydrogen atoms are omitted for clarity.

Compounds **3a** and **3b** feature strong hydrogen bond donors like indole and amide N–H and O–H groups and also strong or moderately strong hydrogen acceptors like C=O, imine N, and  $-\text{O--CH}_3$  groups. Thus, the formation of strong hydrogen bonding interactions is highly possible. Indeed, strong hydrogen bonding interactions of  $\text{N--H}_{\text{amide}} \dots \text{O=C}$ ,  $\text{O--H} \dots \text{O=C}$ , and  $\text{N--H}_{\text{indole}} \dots \text{O--CH}_3$  types are detected for **3a** with H...A distances varying between 1.71–2.10 Å and D-H...A angles between 145–177° (Figure 3a, Table 1).

For compound **3b**, a very strong hydrogen bonding interaction of  $\text{O--H} \dots \text{O=C}$  type ( $d(\text{H} \dots \text{A}) = 1.66 \text{ \AA}$ ,  $D\text{-H--A} = 170^\circ$ ) is observed. Furthermore, weak C–H...O and C–H...N<sub>imine</sub> contacts between the two independent molecules in **3b** are also detected (Figure 3b). The presence of aromatic rings in **3a** and **3b** contributes to the increased chance of  $\pi\text{-}\pi$  stacking interactions. However, staggering (parallel-displaced)  $\pi\text{-}\pi$  stacking interactions are only detected between the 3,4-dihydroxybenzene and indole rings of **3a** (Figure 3c) with a mean plane angle of 8.746°, centroid-to-centroid distance of 3.624 Å, and shift distances of the centroids of  $-1.989 \text{ \AA}$ . In summary, the combination of hydrogen bonding interactions, short contacts, and  $\pi\text{-}\pi$  stacking contributes to the stabilisation and specific three-dimensional packing of the molecules of **3a** and **3b** in the crystal structures. Interestingly, the three-dimensional packing of the molecules of **3b** produces a zigzag layering projected along the *c*-axis (Figure 3d).

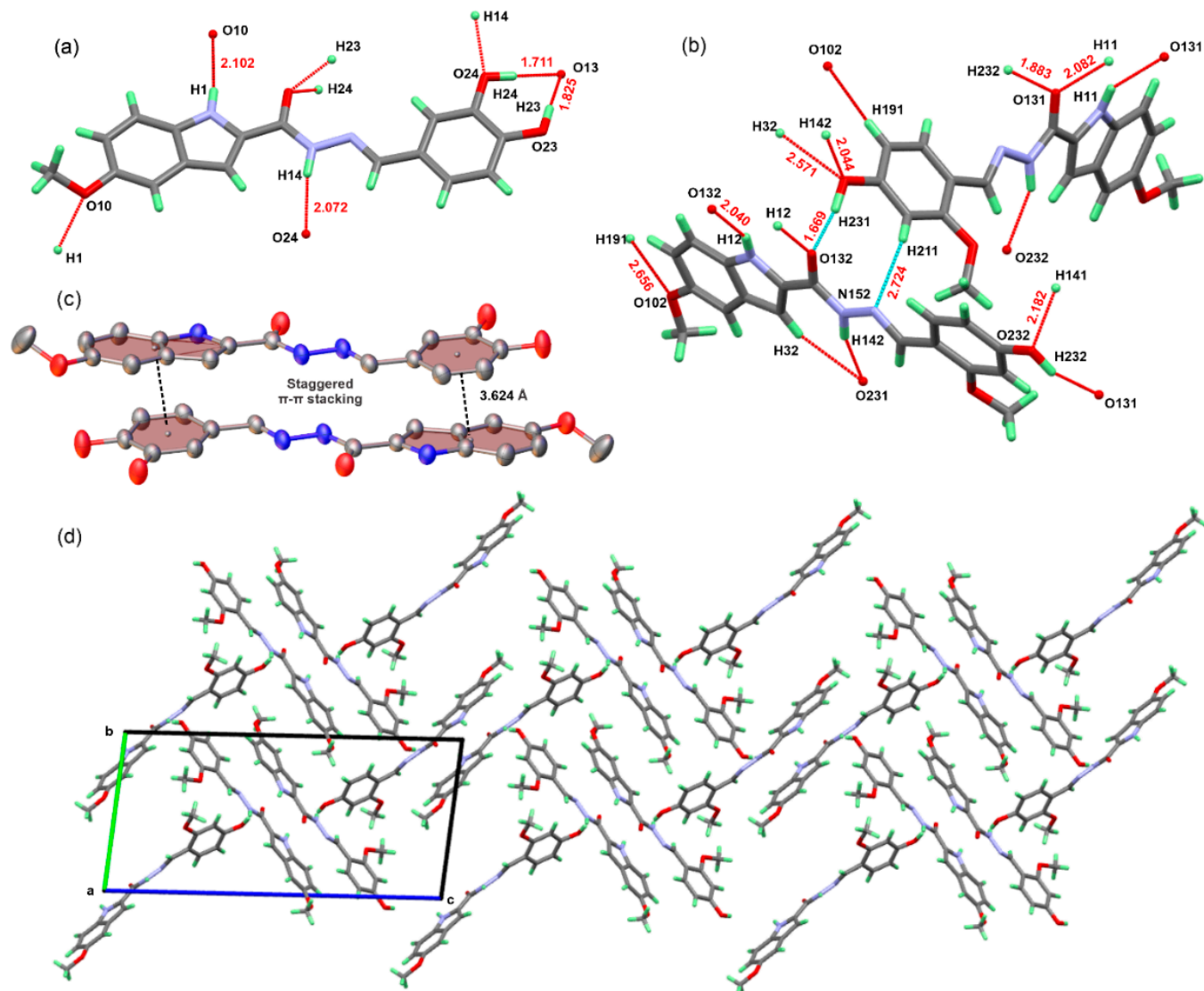


**Figure 3.** Combined representation of the detected hydrogen bonding interactions and short contacts in **3a** (a) and **3b** (b), staggering  $\pi\cdots\pi$  stacking interactions between the 3,4-dihydroxybenzene and indole rings of **3a** (c), and (d) specific three-dimensional packing of the molecules of **3b**, producing zigzag layering along the *c*-axis. Distances are given in Å and hydrogen atoms in light green for clarity.

Nowadays, molecular features and the arrangement of molecules in crystals are extensively studied due to possible applications in crystal engineering and as a tool for explaining molecular and crystalline state characteristics. In the present work, we conducted a Hirshfeld surface analysis (HSA) [42,43] using CrystalExplorer version 21.5 [32], intending to provide valuable insights into the molecular and crystal arrangement of **3a** and **3b**. The HSA produces detailed information about non-covalent interactions (short and long contacts, based on the sum of Van der Waals (VdW) radii, detailed 2D interaction fingerprint plot analysis, shape index, curvedness, interaction energies between the molecular entities, energies frameworks, etc. [31,32]).

For compound **3a**, the Hirshfeld surface (HS) for non-covalent interactions plotted over  $d_{\text{norm}}$  reveals five sites with interatomic contacts shorter than the sum of VdW (Figure 4a, red regions). Those contacts are due to O...H and N...H interactions and are also responsible for the four hydrogen bonds listed in Table 1. The  $\pi\cdots\pi$  staggered stacking, already disclosed in Figure 3c, can be foreseen by plotting HS over the shape index (Figure 4b). The specific contribution of the individual interatomic interactions related to the overall stabilisation of the crystal structure is disclosed by the 2D fingerprint plot analysis in

**Figure 5.** The individual 2D fingerprints disclose that for the stabilisation of **3a**, H...H interactions (36.1%) are the dominant ones. The hydrogen bonding and C-H  $\cdots$   $\pi$  interactions (O...H (24.2%) and N...H (6.2%) and C...H (22.5%)) also have a significant contribution (e.g., 52.9%).

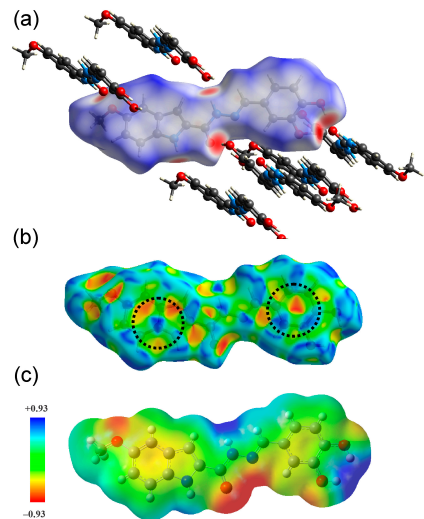


**Figure 4.** Depiction of (a) Hirshfeld surface plotted over  $d_{\text{norm}}$ . Red-coloured regions disclose distance between interacting atoms shorter than sum of VdW radii, blue regions longer than VdW, (b) shape index (from  $-1$  to  $1$  a.u.) disclosing  $\pi \cdots \pi$  staggered stacking interaction dashed circles, and (c) MEP map of **3a**.

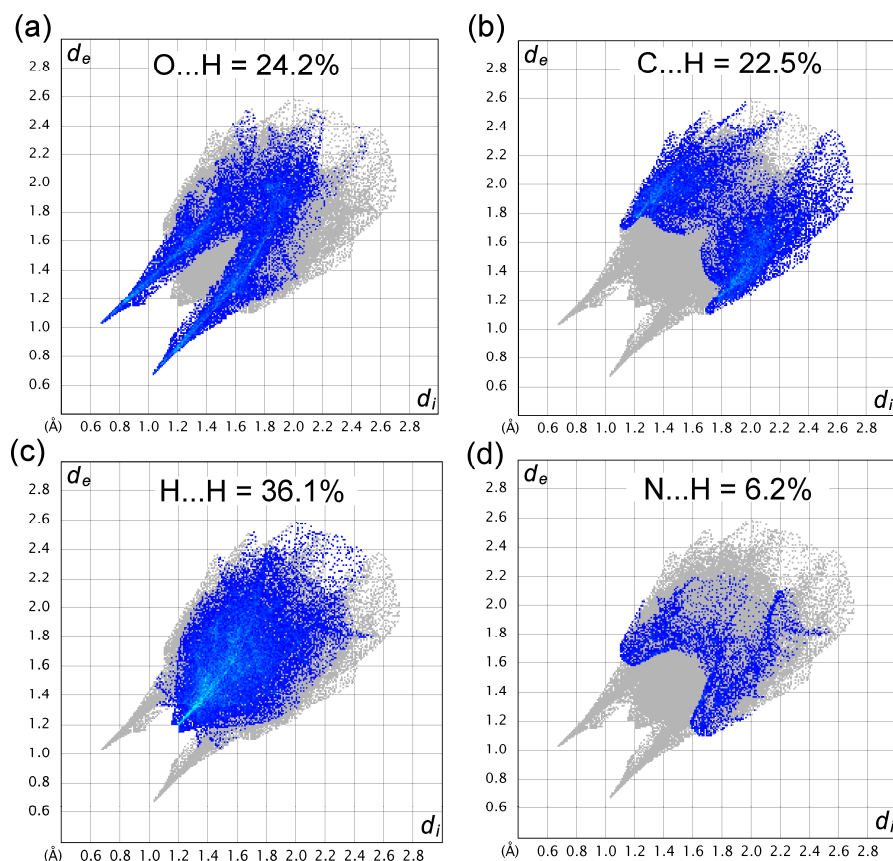


**Figure 5.** Two-dimensional fingerprint plots of major individual interactions observed in **3a** in blue: (a) O-H...O interaction, (b) C...H interaction, (c) H...H interaction and, (d) N-H...O interaction; the overall interaction plot is portrayed in grayish.

The interaction energies (kJ/mol) and energy frameworks in **3a** were calculated in the B3LYP/6-31G(d,p) electron density model with the TONTO program of CrystalExplorer version 21.5, see Figure 6 and Table S6. The electrostatic, polarisation, dispersive, and total energies ( $E_{ele}$ ,  $E_{pol}$ ,  $E_{dis}$ ,  $E_{rep}$ ,  $E_{tot}$ , respectively) are typical for most molecular pairs of molecules in **3a** and can be directly related to hydrogen bonding interactions. The calculation results along with the energy frameworks disclose that the stabilisation of the molecular network is achieved through electrostatic interaction (Figure 6a).

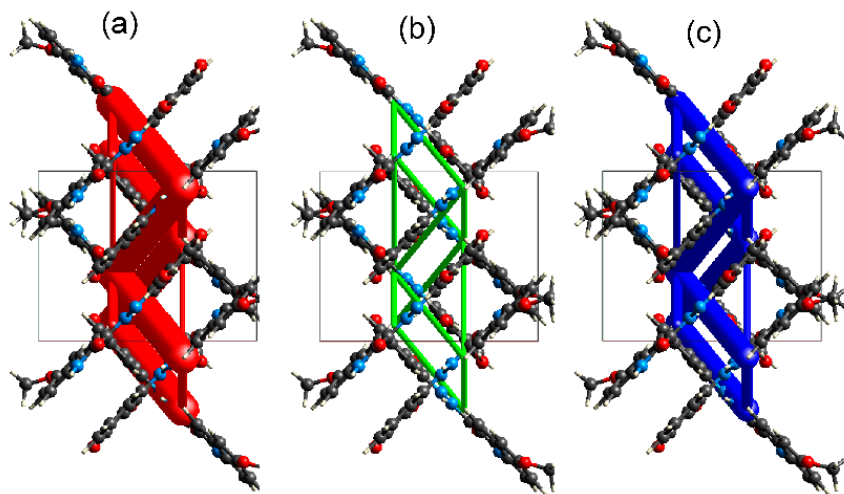


**Figure 6.** Energy framework diagrams for a cluster of nearest-neighbour molecules in **3a** viewed along *c*-axis: (a) electrostatic energy, (b) repulsive energy, and (c) total energy; the cylinder energy scale is identical in all diagrams.

The electrostatic potential map (MEP) of compound **3a** (Figure 4c) discloses two (and possibly up to four) nucleophilic sites and two electrophilic reactive sites in red, electron-rich, negative, and in blue, electron-deficient, positive. The hydrogen near the N14 atom is in an electron-deficient zone (blue colour); thus, it will probably act as an electrophile (H<sub>N14</sub> net atomic charge of +0.321). The situation is similar for the hydrogen atoms near O23 and O24 (net atomic charge of +0.336 and +0.334, respectively). They will have the tendency to absorb electrons from electron-rich species. On the other hand, O13 and O10 are supposedly electron-rich and thus will act as nucleophiles, providing electrons in chemical reactions (net atomic charge of -0.586 and -0.503, respectively). The MEP discloses a few faint red-coloured regions near O23 and O24 and one faint blue-coloured region near N11. The remaining part of **3a** is neutral, i.e., in a stable state. The energy gap between the HOMO and LUMO orbitals (Figure S3) in **3a** is quite low at -0.1567 eV, suggesting that **3a** will be quite reactive.

In **3b**, the HSA has to account for the presence of two molecules in the ASU. The major difference in the two molecules is the orientation of methoxy moiety O101-C111 in molecule 1 (**3b1**) and O102-C112 in molecule 2 (**3b2**), see Figure 2b. Additionally, the 4-hydroxy-2-methoxy benzyl moiety discloses rotational flexibility, i.e., rotamers may be additionally expected. These conformational differences between the two molecules produce a slightly different arrangement of the hydrogen bonding centres, clearly visualised in Figure 7. Similar to compound **3a**, the HS for non-covalent interactions plotted over  $d_{norm}$  reveals four sites with interatomic contacts shorter than the sum of VdW for **3b** (Figure 7a, red regions). The fifth expected contact (related to the 5-methoxy group from the indole moiety) is not detected. This can be perhaps explained by the “mobility” of the methoxy group, existing in dissimilar orientations in the two molecules, and thus preventing the interaction with the “O” acceptor. Also, the N-H and C=O related contacts in the two molecules seem to occur from different sides of the indole mean plane (Figure 7a). Further, the computed shape index of **3b1** and **3b2** does not detect possible sites for C-H· · · π or π· · · π interactions.

The major difference in the shape index of **3b1** and **3b2** is linked to the different orientations of the methoxy group and the “rotation” of the 4-hydroxy-2-methoxy benzyl (Figure 7b).

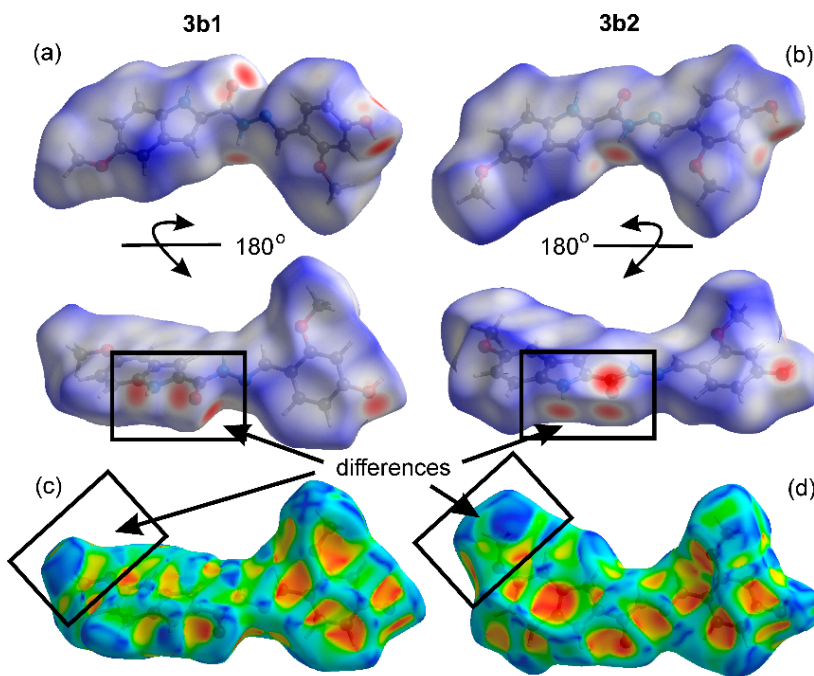


**Figure 7.** Depiction of molecular features of (a) Hirshfeld surface plotted over  $d_{\text{norm}}$ , **3b** molecule 1; red-coloured regions disclose distance between interacting atoms shorter than sum of VdW radii, blue regions longer than VdW, (b) Hirshfeld surface plotted over  $d_{\text{norm}}$ , **3b** molecule 1 and **3b** molecule 2, (c) shape index of **3b** molecule 1 (from  $-1$  to  $1$  a.u.), and (d) shape index of **3b** molecule 1; the most distinct differences between the HSA of the two molecules are pointed out and highlighted by the rectangles.

The specific contribution of the individual interatomic interactions related to the overall stabilisation of the crystal structure of **3b** is disclosed by the 2D fingerprints, see Figure 8. The 2D fingerprints disclose that the stabilisation of **3b** is dominated by  $\text{H} \dots \text{H}$  interactions (40.3%). The hydrogen bonding interactions  $\text{O} \dots \text{H}$  and  $\text{N} \dots \text{H}$  participate with 23.1% and 6.5%, while the  $\text{C} \dots \text{H}$  contribution is 24.0%. These four types of interactions account for 93.9% of the total interactions in **3b**. The results related to the specific individual contribution are very similar to those obtained for compound **3a**. The interaction energies ( $\text{kJ/mol}$ ) and energy frameworks in **3b** were calculated with the B3LYP/6-31G(d,p) electron density model, see Figure 9. In contrast to compound **3a**, in compound **3b**, the repulsion energy seems to be the major one involved in the stabilisation of the crystal structure (Table S7).

The MEPs for **3b** (Figure 10) disclose almost identical features for the two molecules present in the ASU. In both cases, there are two distinct centres: one nucleophilic and one electrophilic in nature. The hydrogen near the O<sub>231</sub> and O<sub>232</sub> atoms is in an electron-deficient zone (blue colour); thus, it will probably act as an electrophile ( $\text{H}_{\text{O}231}$  and  $\text{H}_{\text{O}232}$  net atomic charge of +0.424 and +0.430). On the other hand, O<sub>131</sub> and O<sub>132</sub> are supposedly electron-rich and thus will act as nucleophiles, providing electrons in chemical reactions (net atomic charge of -0.526 and -0.531, respectively). The energy gap between the HOMO and LUMO orbitals (Figure 10) in **3b** is quite low at -0.1458 and -0.1587 eV, suggesting that like **3a**, compound **3b** will be quite reactive.

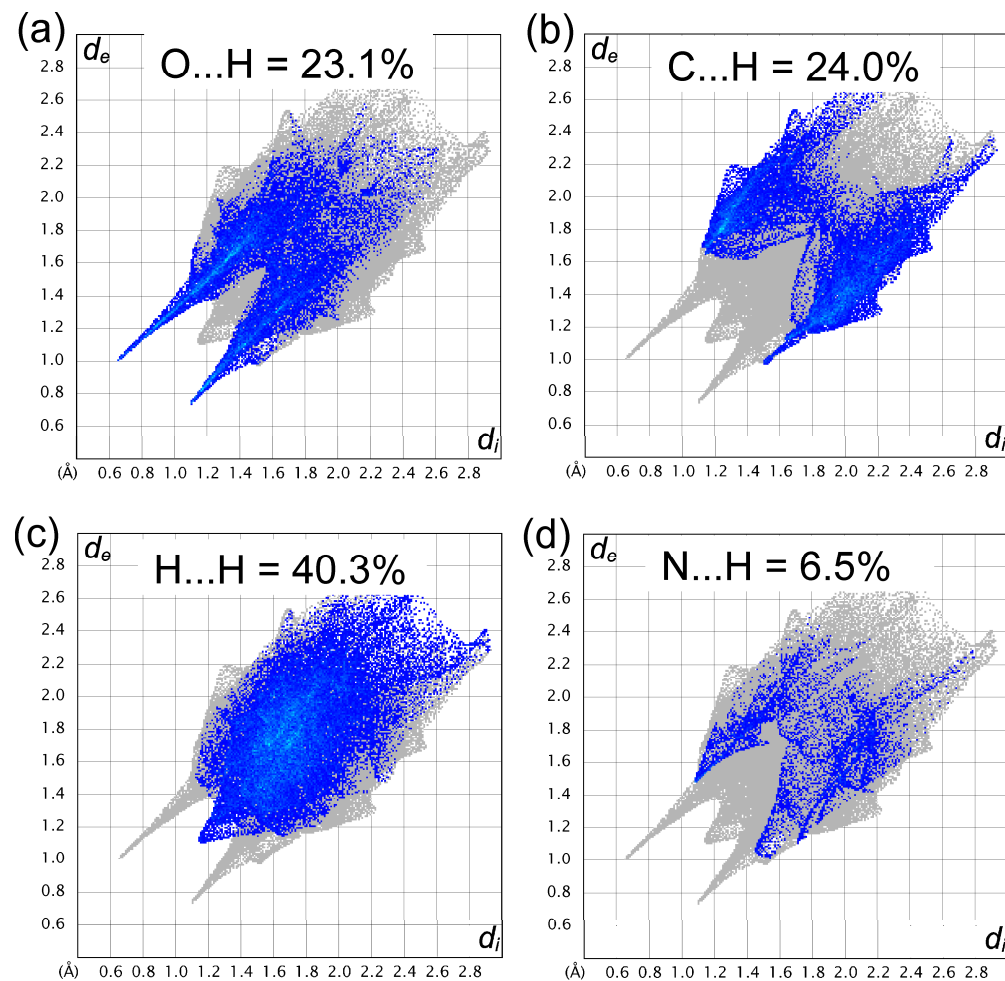


**Figure 8.** Two-dimensional fingerprint plots of major individual interactions (in blue) observed in **3b**: (a) O-H...O interaction, (b) C...H interaction, (c) H...H interaction, and (d) N-H...O interaction; the overall interaction plot is portrayed in grayish.

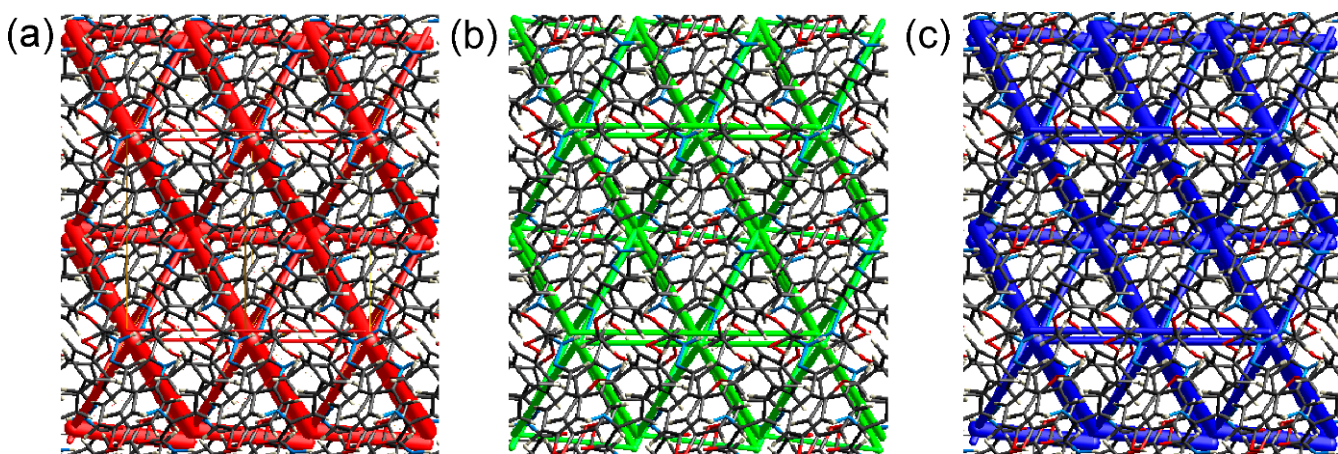


**Figure 9.** Energy framework diagrams for a cluster of nearest-neighbour molecules in **3b** viewed along *c*-axis: (a) electrostatic energy, (b) repulsive energy, and (c) total energy; the cylinder energy scale is identical in all diagrams.

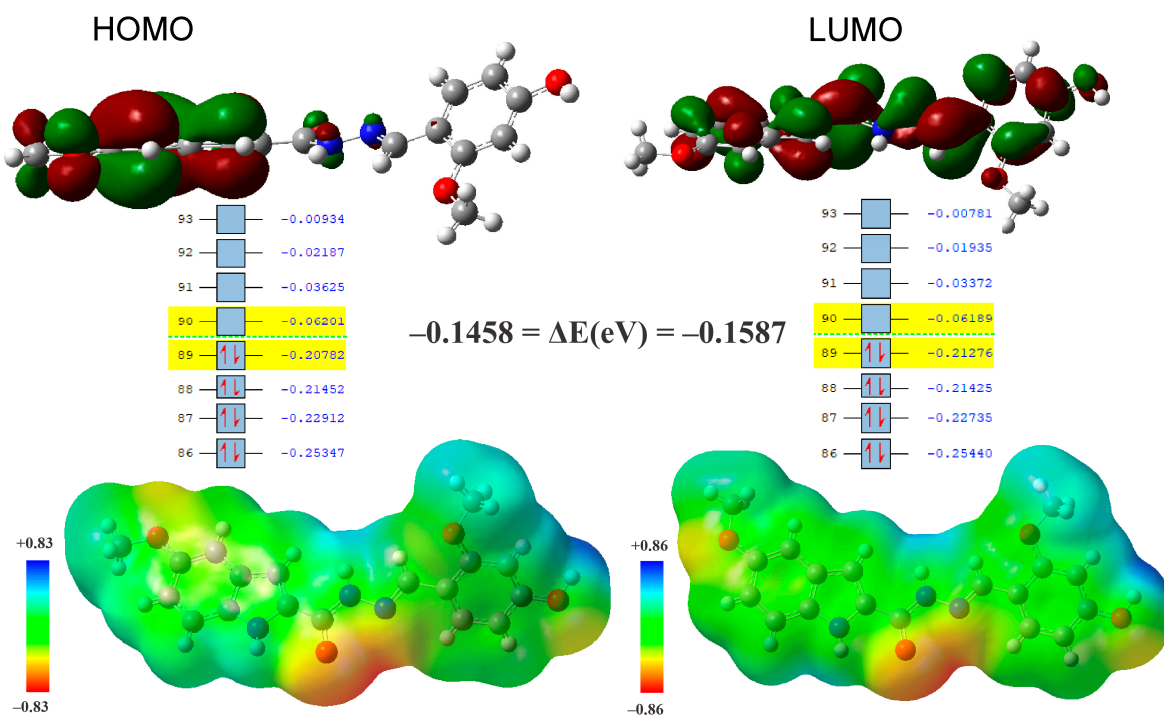


**Figure 10.** MEP map and HOMO/LUMO representation for **3b**.

### 3.3. Evaluation of the Radical Scavenging Activity

In order to shed more light on the influence of the substitution pattern in the arylhydrazone fragments of **3a** and **3b** (3,4-dihydroxyphenyl vs. 2-methoxy-4-hydroxyphenyl moiety) on the pharmacological and, more particularly, the radical scavenging properties of the compounds, we assessed their ability to scavenge superoxide anion radical and hypochlorite ions using luminol-enhances chemiluminescence. The compounds exhibited a concentration-dependent influence on the chemiluminescent scavenging index in all model systems. Specifically, the compounds' effect was evaluated within a concentration range of 1 to 10  $\mu\text{M}$  in the hypochlorite system. The two derivatives under study demonstrated differing effects on the chemiluminescent signal. In the presence of the mono-hydroxy mono-methoxy derivative **3b**, even at the lowest concentration tested (1  $\mu\text{M}$ ), a minimal but statistically significant increase in the chemiluminescent scavenging index was observed compared to the control samples, with a CL-SI of 105% (Figure 11). At the highest test concentration (10  $\mu\text{M}$ ), this increase exceeded 25%. Conversely, the dihydroxy-substituted hydrazone **3a** significantly decreased the chemiluminescent signal to 64% at the lowest concentration tested (1  $\mu\text{M}$ ). At the maximal tested concentration of 10  $\mu\text{M}$ , complete inhibition of the chemiluminescent signal was observed, indicating potent scavenging properties of this compound against the hypochlorite ions.

In the system containing the superoxide anion radical, experiments were conducted at concentrations ranging from 1 to 100  $\mu\text{M}$ . The higher maximal concentration in this model system compared to the previous one was necessitated by the lower reactivity of the superoxide anion radicals compared to hypochlorite ions. Both compounds exhibited the ability to decrease the chemiluminescent scavenging index in a concentration-dependent manner; however, they had varying potency. At concentrations below 5  $\mu\text{M}$ , the determined system parameter for the mono-hydroxy mono-methoxy **3b** was not different from the control sample, indicating a lack of scavenging potential. The scavenging index decreased to 53% for the catechol derivative at a concentration of 5  $\mu\text{M}$ , indicating a potent ability to reduce the concentration of the superoxide anions.

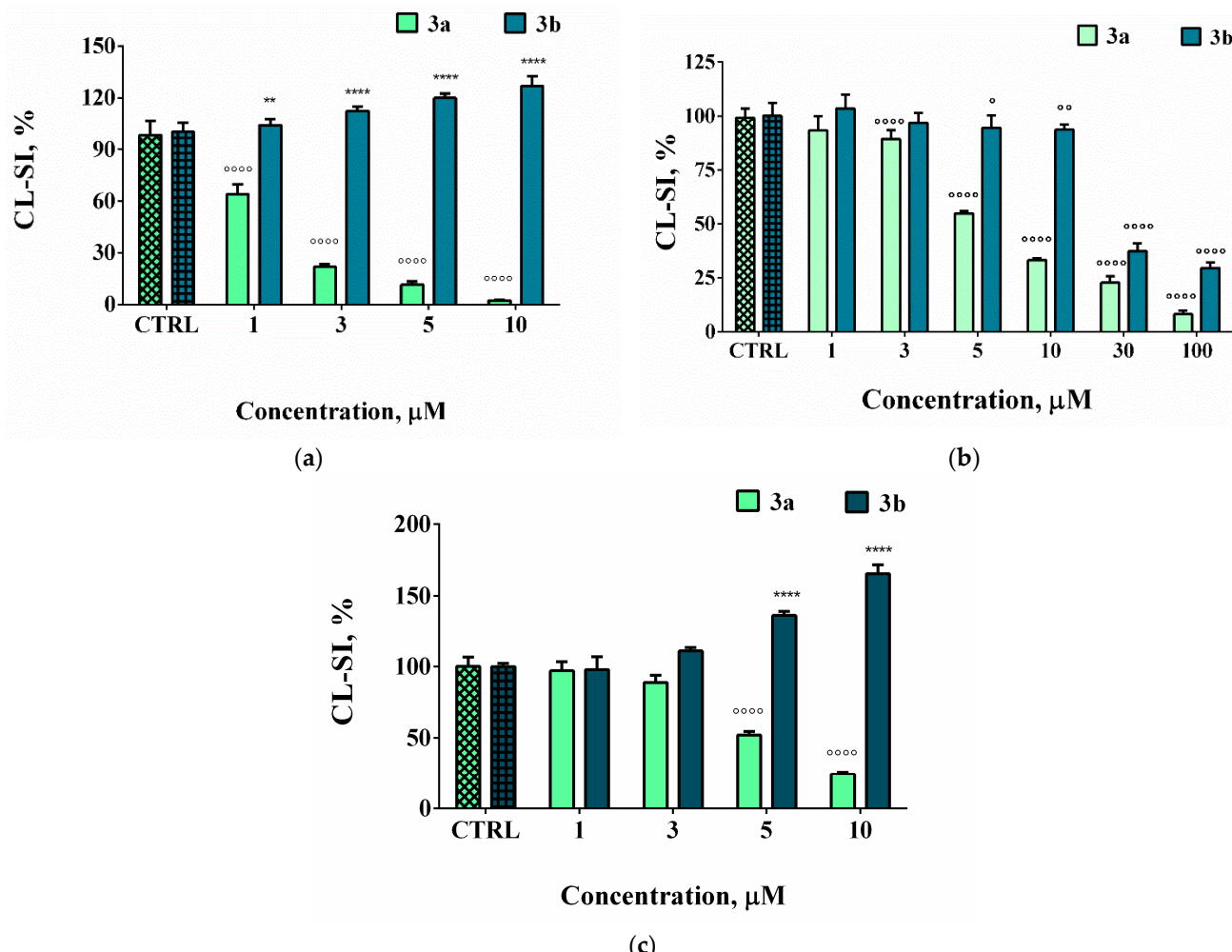


**Figure 11.** Hydrazone derivatives induced modulation of luminol-dependent chemiluminescence in model systems with different ROS: System of NaOCl [0.06mM] generated hypochlorite (a). System of KO<sub>2</sub> produced superoxide (b). System of xanthine—xanthine oxidase generated superoxide (c). The assays were carried out using 1 mL samples of 50 mM PBS containing 0.1 mM luminol. Data are presented from three independent experiments  $\pm$  SEM. With  $^{\circ}$  and  $*$ , significant decreases and increases in the chemiluminescent signal have been marked.  $*/^{\circ} p < 0.05$ ,  $**/^{\circ\circ} p < 0.01$ ,  $^{***}/^{\circ\circ\circ} p < 0.001$ , and  $^{****}/^{\circ\circ\circ\circ} p < 0.0001$  vs. control.

Although both compounds effectively decreased the amount of superoxide anion radicals within the KO<sub>2</sub>-containing system, they displayed opposite effects on the chemiluminescent signal when applied in the xanthine/xanthine oxidase. Notably, the mono-hydroxy mono-methoxy indole **3b** increased the chemiluminescent response at concentrations equal to or exceeding 5  $\mu$ M. Factors such as secondary reactions, alterations in reaction kinetics, or interactions with other components can lead to this outcome, i.e., the apparent increase in the chemiluminescent signal despite the scavenging capability against the superoxide anions. Conversely, the catechol derivative **3a** suppressed the chemiluminescent signal, reducing the CL ratio to approximately 50% at the same concentration as in the enzyme-free model system of superoxide anion generation. At the maximal tested concentration, the estimated parameter was around 25%, which is in accordance with the previously obtained results in the spectrophotometric alternative systems and demonstrates its excellent scavenging activity against the superoxide anion radical [23].

In the second phase of our study, we assessed the potential of the tested derivatives to modulate oxidative damage induced by iron on biologically significant molecules, namely lecithin and deoxyribose. The main advantage of these systems is that they allow for

the evaluation of possible antioxidant and prooxidant effects. Our findings indicate that the tested hydrazones did not exhibit the potential to exacerbate the oxidative damage induced by ferrous iron ions. However, the efficacy of their inhibition on the oxidative damage process depended on both the specific oxidisable substrate utilised and the unique structural features of the derivatives under investigation.

In the system containing lecithin, both compounds demonstrated a statistically significant inhibitory effect on the peroxidation process (Figure 12a). Specifically, the dihydroxy-bearing derivative **3a** exhibited a 66.66% inhibition, while the mono-hydroxy mono-methoxy derivative **3b** showed a 54.73% inhibition. The observed values markedly exceeded those of the reference melatonin (25.94%), indicating a pronounced antioxidant effect. However, while the compounds exhibited potency comparable to the established references Trolox and quercetin, their effect was statistically lower.

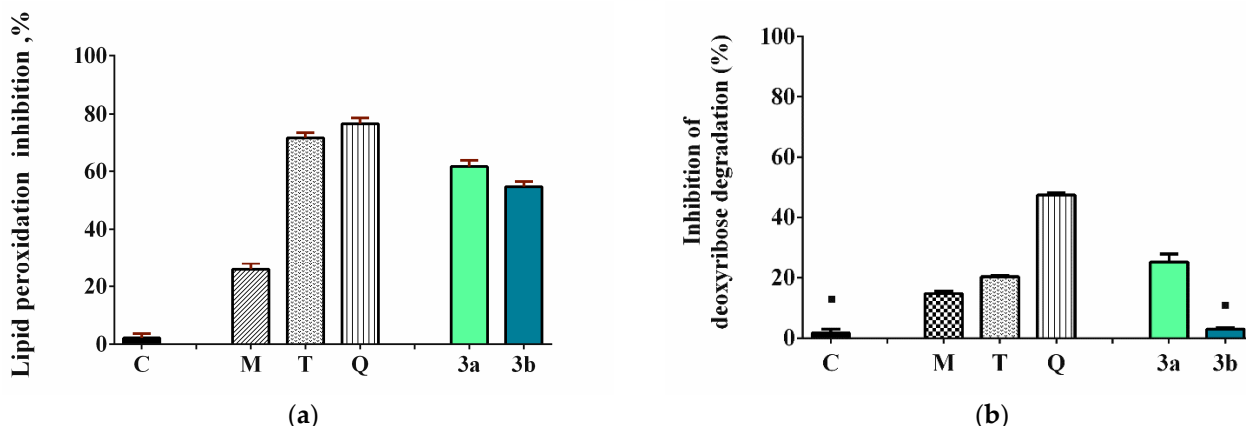


**Figure 12.** Inhibitory effects of the tested hydrazones in model systems of iron-induced oxidative damage evaluated using lecithin at 1 mg/mL (a) and deoxyribose at 0.5 mM (b) as oxidisable substrates. The antioxidant activity of the references melatonin (M), Trolox (T), and quercetin (Q) was also assessed. Data are presented from three independent experiments  $\pm$  SEM. Higher results indicate a more pronounced antioxidant effect. Compounds marked with **I** are considered to have statistically equivalent impact to the control samples.

Both compounds demonstrated diminished inhibitory activity in the deoxyribose degradation assay (Figure 12b). Notably, the observed antioxidant activity was negligible in the mono-hydroxy mono-methoxy derivative **3b** samples. The absorbance values observed were identical to those of the controls, thereby resulting in an inhibition of deoxyribose degradation that approached zero. The catechol derivative **3a** exhibited superior antioxidant properties compared to both melatonin and the potent antioxidant Trolox. Its inhibitory effect on deoxyribose degradation was approximately 25%, which is half the magnitude observed with quercetin.

The findings do not suggest a propensity for triggering a prooxidant effect or ensuing toxicity under the condition of iron-induced oxidative stress, a characteristic feature of neurodegenerative disorders linked to disturbances in iron homeostasis. Nevertheless, in two of the used chemiluminescent systems—the one containing hypochlorite ion and the xanthine–xanthine oxidase—the mono-hydroxy mono-methoxy benzaldehyde derivative stimulated the chemiluminescent response. Hypochlorite ions play a crucial role in the body's defence against pathogenesis. Nevertheless, they are powerful oxidizing agents, and in chronic inflammation or inflammatory disease, the production of hypochlorite ions may be dysregulated [44,45]. The xanthine/xanthine oxidase system is implicated in the natural physiological process involved in purine metabolism, and it is essential for normal physiological functions. Compounds exerting effects such as deregulations or overactivation can lead to oxidative stress. The dihydroxy substituted derivative demonstrated excellent radical scavenging properties in all model systems. The CL-index was below 50%

at concentrations higher than 10  $\mu\text{M}$ . Comparing these data with the results of Oosthuizen et al., we can see that the C-50 values of melatonin were, respectively, for the superoxide and hypochlorite-containing systems, 350  $\mu\text{M}$  and 2500  $\mu\text{M}$ —values much higher than the pharmacological range of serum melatonin and the concentration range tested by us.

Superior radical scavenging properties of dihydroxyphenyl-substituted hydrazones in comparison to other derivatives with hydroxy/methoxy substitution in the phenyl ring were demonstrated previously for hydrazone derivatives of benzimidazole as well [46,47]. Their advantages are related to lower reaction enthalpies for hydrogen atom transfer and proton affinities established by density functional theory (DFT) calculations [47]. Another important aspect that favours the radical scavenging properties of *ortho*-dihydroxy compounds over mono-hydroxy is the different influence of hydrogen bonding with a solvent [48]. Kinetic studies emphasised that while the ability of mono-hydroxy compounds to transfer a hydrogen atom to a free radical would be strongly reduced by the formation of a hydrogen bond with a solvent, the *ortho*-dihydroxy compounds would be still able to react with the second hydroxy group even though it is intramolecularly bonded with the first one [48].

In conclusion, the catechol-containing hydrazone exhibits better radical scavenging and antioxidant properties, making it more suitable for the development of compounds with combined neuroprotective and antioxidant properties.

#### 4. Conclusions

We have carried out a study on the 3,4-dihydroxybenzaldehyde hydrazone derivative of 5MICA and a newly synthesised analogue bearing a 2-methoxy-4-hydroxyphenyl ring using single-crystal X-ray diffraction. It was found that compounds **3a** and **3b** crystallised in the monoclinic  $P2_1/c$  and the triclinic  $P-1$  space groups with one or two independent molecules in the asymmetric unit and a total of four molecules in the unit cell. Despite the presence of a  $-\text{C}(=\text{O})-\text{NH}-\text{N}=\text{CH}-$  bridge, both compounds have highly conserved geometry and limited rotation and deformation freedom of the respective indole and phenyl fragments. Interestingly, a conformational difference between the two independent molecules in the asymmetric unit of **3b** was found. The X-ray study revealed that the specific three-dimensional packing of the molecules of **3a** and **3b** in the crystal structures is stabilised by a combination of hydrogen bonding interactions, short contacts, and  $\pi-\pi$  stacking. The three-dimensional packing of the molecules of **3b** is characterised by a zigzag layering projected along the  $c$ -axis.

The assessment of the ability of the two compounds to scavenge ROS using luminol-enhanced chemiluminescence demonstrated that both compounds effectively decreased luminol-dependent chemiluminescence in model systems with  $\text{KO}_2$ -produced superoxide. However, they displayed opposite effects when applied in a xanthine/xanthine oxidase or hypochlorite system. Notably, in the xanthine/xanthine oxidase system, the 4-hydroxy-2-methoxybenzaldehyde derivative increased the chemiluminescent response at concentrations equal to or exceeding 5  $\mu\text{M}$ , while the 3,4-dihydroxybenzaldehyde derivative suppressed the chemiluminescent signal, reducing the CL ratio to approximately 50% at the same concentration. The potential of the tested derivatives to modulate oxidative damage induced by iron on biologically significant molecules such as lecithin and deoxyribose was evaluated in order to clarify the possible antioxidant and prooxidant effects of the compounds. Our findings do not suggest a propensity of the hydrazones of 5MICA to trigger a prooxidant effect or subsequent toxicity under conditions of iron-induced oxidative stress, a characteristic feature of neurodegenerative disorders linked to disturbances in iron homeostasis. The 3,4-dihydroxy-substituted derivative demonstrated excellent radical scavenging properties in all model systems, making it the lead compound for the development of compounds with combined neuroprotective and antioxidant properties.

**Supplementary Materials:** The following supporting information can be downloaded at: <https://www.mdpi.com/article/10.3390/cryst14050396/s1>, Figure S1: ATR-FTIR spectrum of compound **3b**; Figure S2:  $^1\text{H}$  NMR spectrum of compound **3b** in DMSO-*d*<sub>6</sub>; Figure S3. HOMO/LUMO representation for **3a**; Table S1: Most important crystallographic parameters for the crystal structures of **3a** and **3b**; Table S2: Bond lengths for the crystal structure of **3a**; Table S3: Bond angles for the crystal structure of **3a**; Table S4: Selected bond lengths, angles, and torsion angles for the crystal structure of **3b**; Table S5: Bond angles for the crystal structure of **3b**; Table S6: Interaction energies (kJ/mol) of molecule **3a** computed using single-crystal geometries; Table S7: Interaction energies (kJ/mol) of molecules from **3b** computed using single-crystal geometries.

**Author Contributions:** Conceptualisation, N.A. and D.Y.; Investigation, N.A., N.H.-A. and R.R.; Methodology, N.A., N.H.-A., R.R., B.S. and D.Y.; Supervision, B.S. and D.Y.; Visualisation, N.A., N.H.-A., R.R., B.S. and D.Y.; Writing—original draft, N.A., N.H.-A., R.R., B.S. and D.Y.; Writing—review and editing, N.A., N.H.-A., R.R., B.S. and D.Y. All authors have read and agreed to the published version of the manuscript.

**Funding:** This work is financially supported by the European Union-NextGenerationEU through the National Recovery and Resilience Plan of the Republic of Bulgaria, project no. BG-RRP-2.004-0002, “BiOrgaMCT”. The financial support of the National Science Fund of Bulgaria, young scientists project grant number KP06-M59/2 is gratefully acknowledged.

**Data Availability Statement:** The original contributions presented in the study are included in the article/Supplementary Material, further inquiries can be directed to the corresponding author/s.

**Acknowledgments:** Equipment of INFRAMAT (Research Infrastructure from National Roadmap of Bulgaria), supported by the Bulgarian Ministry of Education and Science, was used in a part of the present investigations.

**Conflicts of Interest:** The authors declare no conflicts of interest.

## References

- Alkhalfaf, L.M.; Ryan, K.S. Biosynthetic manipulation of tryptophan in bacteria: Path-ways and mechanisms. *Chem. Biol.* **2015**, *22*, 317–328. [[CrossRef](#)] [[PubMed](#)]
- Zhang, L.S.; Davies, S.S. Microbial metabolism of dietary components to bioactive metabolites: Opportunities for new therapeutic interventions. *Genome Med.* **2016**, *8*, 46. [[CrossRef](#)] [[PubMed](#)]
- Umer, S.M.; Solangi, M.-H.; Khan, K.M.; Saleem, R.S.Z. Indole-Containing Natural Products 2019–2022: Isolations, Reappraisals, Syntheses, and Biological Activities. *Molecules* **2022**, *27*, 7586. [[CrossRef](#)] [[PubMed](#)]
- Xu, L.L.; Hai, P.; Zhang, S.B.; Xiao, J.F.; Gao, Y.; Ma, B.J.; Fu, H.Y.; Chen, Y.M.; Yang, X.L. Prenylated indole diterpene alkaloids from a mine-soil-derived *Tolyposocladium* sp. *J. Nat. Prod.* **2019**, *82*, 221–231. [[CrossRef](#)] [[PubMed](#)]
- Sim, D.S.; Navanesan, S.; Sim, K.S.; Gurusamy, S.; Lim, S.H.; Low, Y.Y.; Kam, T.S. Conolodinines A–D, Aspidosperma-Aspidosperma bisindole alkaloids with antiproliferative activity from *Tabernaemontana corymbosa*. *J. Nat. Prod.* **2019**, *82*, 850–858. [[CrossRef](#)] [[PubMed](#)]
- Zhou, L.M.; Kong, F.D.; Fan, P.; Ma, Q.Y.; Xie, Q.Y.; Li, J.H.; Zheng, H.Z.; Zheng, Z.H.; Yuan, J.Z.; Dai, H.F.; et al. Indole-diterpenoids with protein tyrosine phosphatase inhibitory activities from the marine-derived fungus *Penicillium* sp. KFD28. *J. Nat. Prod.* **2019**, *82*, 2638–2644. [[CrossRef](#)] [[PubMed](#)]
- França, P.H.B.; Barbosa, D.P.; da Silva, D.L.; Ribeiro, É.A.N.; Santana, A.E.G.; Santos, B.V.O.; Barbosa-Filho, J.M.; Quintans, J.S.S.; Barreto, R.S.S.; Quintans-Júnior, L.J.; et al. Indole Alkaloids from Marine Sources as Potential Leads against Infectious Diseases. *BioMed Res. Int.* **2014**, *2014*, 375423. [[CrossRef](#)] [[PubMed](#)]
- Fernández, S.; Arnáiz, V.; Rufo, D.; Arroyo, Y. Current Status of Indole-Derived Marine Natural Products: Synthetic Approaches and Therapeutic Applications. *Mar. Drugs* **2024**, *22*, 126. [[CrossRef](#)]
- Kiesecker, C.; Zitron, E.; Luck, S.; Bloehs, R.; Scholz, E.P.; Kathofer, S.; Thomas, D.; Kreye, V.A.; Katus, H.A.; Schoels, W.; et al. Class Ia anti-arrhythmic drug ajmaline blocks HERG potassium channels: Mode of action. *Naunyn Schmiedebergs Arch. Pharmacol.* **2004**, *370*, 423–435. [[CrossRef](#)]
- Moore, P.W.; Rasimas, J.J.; Donovan, J.W. Physostigmine is the antidote for anticholinergic syndrome. *J. Med. Toxicol.* **2015**, *11*, 159–160. [[CrossRef](#)]
- Avendaño, C.; Menéndez, J.C. (Eds.) Chapter 8—Anticancer drugs targeting tubulin and microtubules. In *Medicinal Chemistry of Anticancer Drugs*; Elsevier: Amsterdam, The Netherlands, 2008; pp. 229–249.
- Koenig, X.; Hilber, K. The anti-addiction drug ibogaine and the heart: A delicate relation. *Molecules* **2015**, *20*, 2208–2228. [[CrossRef](#)] [[PubMed](#)]

13. De Mello, V.D.; Paananen, J.; Lindström, J.; Lankinen, M.A.; Shi, L.; Kuusisto, J.; Pihlajamäki, J.; Auriola, S.; Lehtonen, M.; Rolandsson, O.; et al. Indolepropionic acid and novel lipid metabolites are associated with a lower risk of type 2 diabetes in the Finnish diabetes prevention study. *Sci. Rep.* **2017**, *7*, 46337. [CrossRef] [PubMed]
14. Tuomainen, M.; Tuomainen, M.; Lindström, J.; Lehtonen, M.; Auriola, S.; Pihlajamäki, J.; Peltonen, M.; Tuomilehto, J.; Uusitupa, M.; de Mello, V.D.; et al. Associations of serum indolepropionic acid, a gut microbiota metabolite, with type 2 diabetes and low-grade inflammation in high-risk individuals. *Nutr. Diabetes* **2018**, *8*, 4–8. [CrossRef] [PubMed]
15. Westfall, S.; Iqbal, U.; Sebastian, M.; Pasinetti, G.M. Gut microbiota mediated allosterism prevents stress-induced neuroinflammatory risk factors of Alzheimer’s disease. *Prog. Mol. Biol. Transl. Sci.* **2019**, *168*, 147–181. [PubMed]
16. Pappolla, M.A.; Matsubara, E.; Vidal, R.; Pacheco-Quinto, J.; Poeggeler, B.; Zagorski, M.; Sambamurti, K. Melatonin treatment enhances A $\beta$  lymphatic clearance in a transgenic mouse model of amyloidosis. *Curr. Alzheimer Res.* **2018**, *15*, 637–642. [CrossRef] [PubMed]
17. Bruno, V. Targeting the aryl hydrocarbon receptor with Indole-3-aldehyde protects from Vulvovaginal candidiasis via the IL-22-IL-18. *Front. Immunol.* **2019**, *10*, 2364.
18. Pappolla, M.A.; Perry, G.; Fang, X.; Zagorski, M.; Sambamurti, K.; Poeggeler, B. Indoles as essential mediators in the gut-brain axis. Their role in Alzheimer’s disease. *Neurobiol. Dis.* **2021**, *156*, 105403. [CrossRef] [PubMed]
19. Poeggeler, B.; Sambamurti, K.; Siedlak, S.L.; Perry, G.; Smith, M.A.; Pappolla, M.A. A novel endogenous indole protects rodent mitochondria and extends rotifer lifespan. *PLoS ONE* **2010**, *5*, e10206. [CrossRef]
20. Sumien, N.; Huang, R.; Chen, Z.; Vann, P.H.; Wong, J.M.; Li, W.; Yang, S.; Forster, M.J.; Yan, L.J. Effects of dietary 5-methoxyindole-2-carboxylic acid on brain functional recovery after ischemic stroke. *Behav. Brain Res.* **2020**, *378*, 112278. [CrossRef]
21. Wu, J.; Li, R.; Li, W.; Ren, M.; Thangthaeng, N.; Sumien, N.; Liu, R.; Yang, S.; Simpkins, J.W.; Forster, M.J.; et al. Administration of 5-methoxyindole-2-carboxylic acid that potentially targets mitochondrial dihydrolipoamide dehydrogenase confers cerebral preconditioning against ischemic stroke injury. *Free Radic. Biol. Med.* **2017**, *113*, 244–254. [CrossRef]
22. Wu, J.; Jin, Z.; Yang, X.; Yan, L.J. Post-ischemic administration of 5-methoxyindole-2-carboxylic acid at the onset of reperfusion affords neuroprotection against stroke injury by preserving mitochondrial function and attenuating oxidative stress. *Biochem. Biophys. Res. Commun.* **2018**, *497*, 444–450. [CrossRef] [PubMed]
23. Anastassova, N.; Stefanova, D.; Hristova-Avakumova, N.; Georgieva, I.; Kondeva-Burdina, M.; Rangelov, M.; Todorova, N.; Tzoneva, R.; Yancheva, D. New Indole-3-Propionic Acid and 5-Methoxy-Indole Carboxylic Acid Derived Hydrazone Hybrids as Multifunctional Neuroprotectors. *Antioxidants* **2023**, *12*, 977. [CrossRef] [PubMed]
24. Bruker AXS Inc. *Apex 4. Bruker Advanced X-ray Solutions*; Bruker AXS Inc.: Madison, WI, USA, 2022.
25. Bruker APEX, version 2021.10.0, Saint and Sadabs; Bruker AXS Inc.: Madison, WI, USA, 2009.
26. Sheldrick, G.M. Shelxt—Integrated Space-Group and Crystal-Structure Determination. *Acta Crystallogr. A* **2015**, *71*, 3–8. [CrossRef] [PubMed]
27. Sheldrick, G.M. Crystal Structure Refinement with Shelxl. *Acta Crystallogr. C* **2015**, *71*, 3–8. [CrossRef] [PubMed]
28. Dolomanov, O.V.; Bourhis, L.J.; Gildea, R.J.; Howard, J.A.K.; Puschmann, H. Olex2: A Complete Structure Solution, Refinement and Analysis Program. *J. Appl. Crystallogr.* **2009**, *42*, 339–341. [CrossRef]
29. Farrugia, L.J. Wingx and Ortep for Windows: An Update. *J. Appl. Crystallogr.* **2012**, *45*, 849–854. [CrossRef]
30. Macrae, C.F.; Sovago, I.; Cottrell, S.J.; Galek, P.T.A.; McCabe, P.; Pidcock, E.; Platings, M.; Shields, G.P.; Stevens, J.S.; Towler, M. Mercury 4.0: From Visualization to Analysis, Design and Prediction. *J. Appl. Crystallogr.* **2020**, *53*, 226–235. [CrossRef] [PubMed]
31. Mackenzie, C.F.; Spackman, P.R.; Jayatilaka, D.; Spackman, M.A. CrystalExplorer model energies and energy frameworks: Extension to metal coordination compounds, organic salts, solvates and open-shell systems. *IUCrJ* **2017**, *4*, 575–587. [CrossRef] [PubMed]
32. Spackman, P.R.; Turner, M.J.; McKinnon, J.J.; Wolff, S.K.; Grimwood, D.J.; Jayatilaka, D.; Spackman, M.A. CrystalExplorer: A program for Hirshfeld surface analysis, visualization and quantitative analysis of molecular crystals. *J. Appl. Crystallogr.* **2021**, *54*, 1006–1011. [CrossRef]
33. Jayatilaka, D.; Grimwood, D.J. Tonto: A fortran based object-oriented system for quantum chemistry and crystallography. In *International Conference on Computational Science*; Springer: Berlin/Heidelberg, Germany, 2003; pp. 142–151.
34. Van Dyke, K.; Van Dyke, C.; Woodfork, K. (Eds.) *Luminescence biotechnology: Instruments and Applications*; CRC Press: Boca Raton, FL, USA, 2002.
35. Roda, A.; Guardigli, M.; Pasini, P. Bioluminescence and chemiluminescence in drug screening. *Anal. Bioanal. Chem.* **2003**, *377*, 826–833. [CrossRef]
36. Tzani, M.A.; Gioftsidou, D.K.; Kallitsakis, M.G.; Pliatsios, N.V.; Kalogiouri, N.P.; Angaridis, P.A.; Lykakis, I.N.; Terzidis, M.A. Direct and Indirect Chemiluminescence: Reactions, Mechanisms and Challenges. *Molecules* **2021**, *26*, 7664. [CrossRef] [PubMed]
37. Ghani, M.A.; Barril, C.; Bedgood, D.R.; Prenzler, P.D. Measurement of antioxidant activity with the thiobarbituric acid reactive substances assay. *Food Chem.* **2017**, *230*, 195–207. [CrossRef] [PubMed]
38. Anastassova, N.; Aluani, D.; Hristova-Avakumova, N.; Tzankova, V.; Kondeva-Burdina, M.; Rangelov, M.; Todorova, N.; Yancheva, D. Study on the Neuroprotective, Radical-Scavenging and MAO-B Inhibiting Properties of New Benzimidazole Arylhydrazones as Potential Multi-Target Drugs for the Treatment of Parkinson’s Disease. *Antioxidants* **2022**, *11*, 884. [CrossRef]
39. Wang, G.; Wang, T. Oxidative stability of egg and soy lecithin as affected by transition metal ions and pH in emulsion. *J. Agric. Food Chem.* **2008**, *56*, 11424–11431. [CrossRef] [PubMed]

40. Sadowska-Bartosz, I.; Galiniak, S.; Bartosz, G. Modification of the deoxyribose test to detect strong iron binding. *Acta Biochim. Pol.* **2017**, *64*, 195–198. [[CrossRef](#)] [[PubMed](#)]
41. Chobot, V.; Hadacek, F.; Bachmann, G.; Weckwerth, W.; Kubicova, L. In Vitro Evaluation of Pro- and Antioxidant Effects of Flavonoid Tricetin in Comparison to Myricetin. *Molecules* **2020**, *25*, 5850. [[CrossRef](#)] [[PubMed](#)]
42. Spackman, M.A.; Jayatilaka, D. Hirshfeld surface analysis. *Cryst. Eng. Comm.* **2009**, *11*, 19–32. [[CrossRef](#)]
43. McKinnon, J.J.; Jayatilaka, D.; Spackman, M.A. Towards quantitative analysis of intermolecular interactions with Hirshfeld surfaces. *Chem. Commun.* **2007**, *7*, 3814–3816. [[CrossRef](#)]
44. Andrés, C.M.C.; Pérez de la Lastra, J.M.; Juan, C.A.; Plou, F.J.; Pérez-Lebeña, E. Hypochlorous Acid Chemistry in Mammalian Cells—Influence on Infection and Role in Various Pathologies. *Int. J. Mol. Sci.* **2022**, *23*, 10735. [[CrossRef](#)]
45. Oosthuizen, M.M.; Greyling, D. Antioxidants suitable for use with chemiluminescence to identify oxyradical species. *Redox Rep.* **1999**, *4*, 277–290. [[CrossRef](#)]
46. Anastassova, N.; Aluani, D.; Kostadinov, A.; Rangelov, M.; Todorova, N.; Hristova-Avakumova, N.; Argirova, M.; Lumov, N.; Kondeva-Burdina, M.; Tzankova, V.; et al. Evaluation of the combined activity of benzimidazole arylhydrazones as new anti-Parkinsonian agents: Monoamine oxidase-B inhibition, neuroprotection and oxidative stress modulation. *Neural. Regen. Res.* **2021**, *16*, 2299–2309. [[CrossRef](#)] [[PubMed](#)]
47. Argirova, M.A.; Georgieva, M.K.; Hristova-Avakumova, N.G.; Vuchev, D.I.; Popova-Daskalova, G.V.; Anichina, K.K.; Yancheva, D.Y. New 1H-benzimidazole-2-yl hydrazones with combined antiparasitic and antioxidant activity. *RSC Adv.* **2021**, *11*, 39848–39868. [[CrossRef](#)] [[PubMed](#)]
48. Foti, M.; Ruberto, G. Kinetic Solvent Effects on Phenolic Antioxidants Determined by Spectrophotometric Measurements. *J. Agric. Food Chem.* **2001**, *49*, 342–348. [[CrossRef](#)] [[PubMed](#)]

**Disclaimer/Publisher's Note:** The statements, opinions and data contained in all publications are solely those of the individual author(s) and contributor(s) and not of MDPI and/or the editor(s). MDPI and/or the editor(s) disclaim responsibility for any injury to people or property resulting from any ideas, methods, instructions or products referred to in the content.